

# pH-Dependent Conformation, Dynamics, and Aromatic Interaction of the Gating Tryptophan Residue of the Influenza M2 Proton Channel from Solid-State NMR

Jonathan K. Williams, Yuan Zhang, Klaus Schmidt-Rohr, and Mei Hong\*

Department of Chemistry, Iowa State University, Ames, Iowa

**ABSTRACT** The M2 protein of the influenza virus conducts protons into the virion under external acidic pH. The proton selectivity of the tetrameric channel is controlled by a single histidine (His<sup>37</sup>), whereas channel gating is accomplished by a single tryptophan (Trp<sup>41</sup>) in the transmembrane domain of the protein. Aromatic interaction between these two functional residues has been previously observed in Raman spectra, but atomic-resolution evidence for this interaction remains scarce. Here we use high-resolution solid-state NMR spectroscopy to determine the side-chain conformation and dynamics of Trp<sup>41</sup> in the M2 transmembrane peptide by measuring the Trp chemical shifts, His<sup>37</sup>-Trp<sup>41</sup> distances, and indole dynamics at high and low pH. The interatomic distances constrain the Trp<sup>41</sup> side-chain conformation to *trans* for  $\chi_1$  and 120–135° for  $\chi_2$ . This *t90* rotamer points the N $\epsilon$ 1-C $\epsilon$ 2-C $\zeta$ 2 side of the indole toward the aqueous pore. The precise  $\chi_1$  and  $\chi_2$  angles differ by ~20° between high and low pH. These differences, together with the known changes in the helix tilt angle between high and low pH, push the imidazole and indole rings closer together at low pH. Moreover, the measured order parameters indicate that the indole rings undergo simultaneous  $\chi_1$  and  $\chi_2$  torsional fluctuations at acidic pH, but only restricted  $\chi_1$  fluctuations at high pH. As a result, the Trp<sup>41</sup> side chain periodically experiences strong cation- $\pi$  interactions with His<sup>37</sup> at low pH as the indole sweeps through its trajectory, whereas at high pH the indole ring is further away from the imidazole. These results provide the structural basis for understanding how the His<sup>37</sup>-water proton exchange rate measured by NMR is reduced to the small proton flux measured in biochemical experiments. The indole dynamics, together with the known motion of the imidazolium, indicate that this compact ion channel uses economical side-chain dynamics to regulate proton conduction and gating.

## INTRODUCTION

The influenza A M2 protein forms a homo-tetrameric proton channel that acidifies the virus after endocytosis (1–3) and maintains the high pH of the Golgi network for proper hemagglutinin function (4). M2 also mediates virus budding from the host cell by causing membrane scission (5). The proton channel is activated by low pH of the external environment, which is presented by the endosome during endocytosis. A conserved HxxxW motif is responsible for unidirectional proton conduction from the exterior into the virion. In this HxxxW motif, His<sup>37</sup> is now known from solid-state NMR data to exchange protons with water molecules at a rate of 10<sup>5</sup> s<sup>-1</sup>, facilitated by small-angle ring reorientations on the same timescale (6,7). The histidine side chain adopts the *trans-trans* conformation for the  $\chi_1$  and  $\chi_2$  torsion angles, such that N $\delta$ 1 and N $\epsilon$ 2 point toward the N- and C-termini of the channel, respectively, primed to accept and release protons. The single-channel proton conductivity is the highest when three out of four histidines of the tetramer are protonated, which occur with a pK<sub>a</sub> of 4.9 in cholesterol-rich virus-mimetic lipid membranes (7). The water-His<sup>37</sup> proton transfer is facilitated by an extensive network of imidazole-water hydrogen

bonds at acidic pH (6,8), but the hydrogen-bonding network is incomplete at high pH, when the channel is closed.

Whereas His<sup>37</sup> is the proton-selective residue, Trp<sup>41</sup> is the gating residue, blocking diffusion of protons from inside the virus but not from the outside (9). Electrophysiology data show that when  $pH_{out}$  is lower than  $pH_{in}$ , there is robust inward proton flux, which is much larger than the outward current when the situation is reversed. This asymmetry is lost when Trp<sup>41</sup> is replaced by other amino-acid residues except Tyr, which also has an electron-rich aromatic ring capable of forming cation- $\pi$  interactions with His<sup>37</sup>. These results suggest that when the Trp<sup>41</sup> gate is closed, protons cannot rapidly access His<sup>37</sup> from inside the virus, thus outward flux is slow under low  $pH_{in}$  and high  $pH_{out}$ .

Despite these functional data on the role of Trp<sup>41</sup> in the channel activity, high-resolution structural information about pH-dependent His<sup>37</sup>-Trp<sup>41</sup> aromatic interaction is still scarce, and the Trp<sup>41</sup> side-chain conformation is still unresolved. Various high-resolution structures of M2 domains showed divergent Trp<sup>41</sup> rotamers that placed the indole ring at varying positions relative to the pore (Table 1). Most structural models found the  $\chi_1$  angle to be *trans* (*t*) but differed on whether the  $\chi_2$  angle is positive or negative 100°. <sup>19</sup>F spin diffusion NMR experiments of 5-<sup>19</sup>F (H $\zeta$ 3)-labeled Trp<sup>41</sup> in the M2 transmembrane peptide (M2TM) (10) found nearest-neighbor <sup>19</sup>F-<sup>19</sup>F distances of ~11 Å at both high and low pH, suggesting a *t90* rotamer, which points the five-membered nitrogen-containing pyrrole ring

Submitted January 16, 2013, and accepted for publication February 11, 2013.

\*Correspondence: mhong@iastate.edu

Editor: Paulo Almeida.

© 2013 by the Biophysical Society  
0006-3495/13/04/1698/11 \$2.00

<http://dx.doi.org/10.1016/j.bpj.2013.02.054>



**TABLE 1** Trp<sup>41</sup> rotamers in various structures of the influenza M2 peptides, solved at different pH, in different membrane-mimetic solvents, using different protein constructs and biophysical methods

PDB ID	pH	Lipid/detergent	Method	Construct	Trp <sup>41</sup> ( $\chi_1$ , $\chi_2$ )
1NYJ	7.0	DMPC	SSNMR	22–46	180°, -105°
2H95	8.8	DMPC	SSNMR	22–46	-100°, 110°
2L0J	7.5	DOPC/DOPE	MD, SSNMR	22–62	180°, -70°
2KAD	7.5	DLPC	SSNMR	22–46	180°, 90°
2KQT	7.5	DMPC	SSNMR	22–46	180°, 90°
3C9J	5.3	Octylglucoside	X-ray	22–46, G34A	180°, 90°
3LBW	6.5	Octylglucoside	X-ray	22–46, G34A	180°, 90°
2RLF	7.5	DHPC	Solution NMR	18–60	160°, -120°
2KWX	7.5	DHPC	Solution NMR	18–60, V27A	180°, -90°
2KIH	7.5	DHPC	Solution NMR	18–60, S31N	180°, -115°

DHPC, Dihexanoylphosphatidylcholine.

toward the channel pore (Fig. 1 *a*). Crystal structures of M2TM at pH 6.5 and pH 5.3 also concluded the *t*90 rotamer (11,12). In comparison, an earlier solid-state NMR measurement of the His<sup>37</sup> N $\epsilon$ 2-Trp<sup>41</sup> C $\gamma$  distance in M2TM found a distance upper limit of 3.9 Å, which was interpreted to constrain the Trp rotamer to *t*-105 ( $\chi_1 = 180^\circ$ ,  $\chi_2 = -105^\circ$ ) (13) (Fig. 1 *b*). The negative  $\chi_2$  angle points

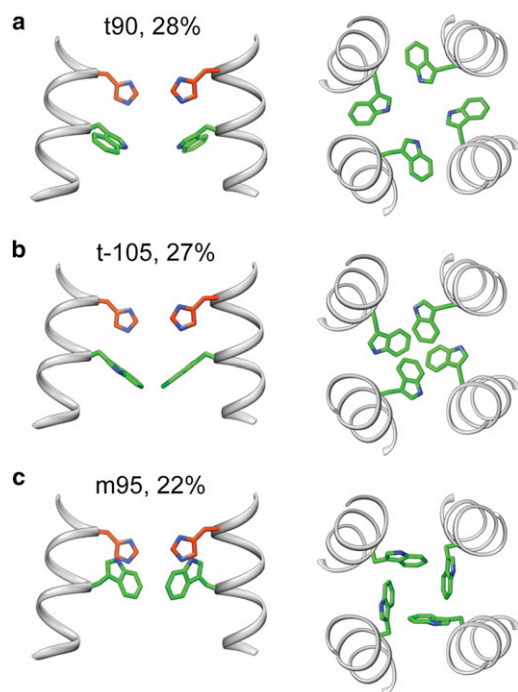


**FIGURE 1** Several Trp<sup>41</sup> rotamers that have been proposed in the literature using various experimental techniques (Table 1). Population percentages for  $\alpha$ -helices from the Penultimate Rotamer Library are shown (42). (Left column) Side view of two of the four helices; both His<sup>37</sup> and Trp<sup>41</sup> side chains are depicted. Note the shortest distances between these two residues are between two adjacent helices rather than from the same helix. (Right column) Top view of the four helices and the Trp<sup>41</sup> sidechains. (a) *t*90 rotamer ( $\chi_1 = 180^\circ$ ,  $\chi_2 = +90^\circ$ ). (b) *t*-105 rotamer ( $\chi_1 = 180^\circ$ ,  $\chi_2 = -105^\circ$ ). (c) *m*95 rotamer ( $\chi_1 = -60^\circ$ ,  $\chi_2 = +95^\circ$ ).

the six-membered benzene ring toward the center of the channel, occluding the pore. Solution NMR structures of a combined transmembrane (TM) and cytoplasmic helix domain of wild-type and mutant M2 proteins also concluded the Trp<sup>41</sup> rotamer to be *t*-105 based on the side-chain J-couplings, residual dipolar couplings, and nuclear Overhauser effects (14,15). Finally, a <sup>19</sup>F NMR study of the lineshapes of 6-<sup>19</sup>F (H $\eta$ 2) Trp<sup>41</sup> in M2TM (16) found a nearest-neighbor <sup>19</sup>F-<sup>19</sup>F distance of ~8.0 Å at low pH and ~3.2 Å at high pH, which led to the proposal of a positive  $\chi_2$  of +100°, but a negative  $\chi_1$  of -100° and -50° for the high- and low-pH states, respectively (Fig. 1 *c*).

Direct experimental evidence of His<sup>37</sup>-Trp<sup>41</sup> aromatic interactions so far mainly comes from ultraviolet resonance Raman spectra, which showed Trp<sup>41</sup> intensity changes at certain wavenumbers at low pH (17). These changes were attributed to cation- $\pi$  interactions between the imidazolium and the indole rings, whereas environmental hydrophobicity and indole hydrogen bonding were ruled out. A recent molecular dynamics simulation that modeled the HxxxW segment led to the proposal that cation- $\pi$  interactions at low pH disrupted a low-barrier hydrogen bond between a cationic and neutral histidine (18), thus activating the channel. However, measured chemical shifts of the protons bonded to the imidazole nitrogens indicate regular His-water hydrogen bonds (8) rather than direct His-His hydrogen bonds.

In this work, we investigate the conformation and dynamics of Trp<sup>41</sup> in M2TM by measuring the Trp<sup>41</sup> chemical shifts, His<sup>37</sup>-Trp<sup>41</sup> distances, and indole dynamics as a function of pH. We show that Trp<sup>41</sup> adopts the *t*90 conformation at both high and low pH, but the exact  $\chi_1$  and  $\chi_2$  angles differ by ~20°. These torsion angle differences, together with the known increase in the helix tilt angle at low pH, push the imidazole of one helix toward the indole of the neighboring helix at low pH. Moreover, measured order parameters indicate that the indole ring undergoes Gaussian fluctuations around both the  $\chi_1$  and  $\chi_2$  bonds at low pH, which further promote His-Trp interaction. These results give fresh insight into the coordinated motion between His<sup>37</sup> and Trp<sup>41</sup> that regulates proton conduction and channel gating.

## MATERIALS AND METHODS

### Membrane peptide samples

The TM segment (residues 22–46: SSDPLVVAASII GILHLILWILDRL) of the Udorn strain of the influenza A M2 protein was synthesized by Primm-Biotech (Cambridge, MA). Two isotopically labeled M2TM peptides were synthesized, one containing uniformly <sup>13</sup>C-, <sup>15</sup>N-labeled Leu<sup>40</sup> and Trp<sup>41</sup> (LW-M2TM) and the other containing <sup>13</sup>C-, <sup>15</sup>N-labeled Gly<sup>34</sup>, His<sup>37</sup>, and 5-<sup>19</sup>F-labeled Trp<sup>41</sup> (GHW-M2TM).

Two virus-mimetic lipid membranes were used to reconstitute the peptides (19,20). The VM membrane consists of DPPC (1,2-dipalmitoyl-*sn*-glycero-3-phosphocholine), DPPE (1,2-dipalmitoyl-*sn*-glycero-3-phosphoethanolamine), SM (egg sphingomyelin), and Chol (cholesterol) at a

molar ratio of 21:21:28:30%, whereas the VM+ membrane consists of POPC (1-palmitoyl-2-oleoyl-*sn*-glycero-3-phosphocholine), POPE (1-palmitoyl-2-oleoyl-*sn*-glycero-3-phosphoethanolamine), SM, and Chol at a molar ratio of 25.6:25.6:25.6: 23%. The VM+ membrane is more dynamic than the VM membrane due to the use of chain-unsaturated phospholipids. For both membranes the lipids and cholesterol were dissolved in chloroform, SM was dissolved in chloroform/methanol solution, and all components were combined at the desired molar ratios. The lipid mixture was dried under a stream of nitrogen gas, redissolved in cyclohexane, and lyophilized overnight. The resulting dry lipid powder was resuspended in the appropriate buffer, vortexed, and subject to 8–10 cycles of freeze-thawing to produce uniform vesicles. Lipid solutions were prepared at two different pH: the pH 8.5 sample used a 10 mM Tris buffer (10 mM Tris, 1 mM EDTA, 0.1 mM Na<sub>2</sub>N<sub>3</sub>) whereas the pH 4.5 sample used a 10 mM citric acid buffer (10 mM citric acid/sodium citrate, 1 mM EDTA, and 0.1 mM Na<sub>2</sub>N<sub>3</sub>).

M2TM was reconstituted into the lipid membrane by detergent dialysis. The peptide was dissolved in an octyl- $\beta$ -D-glucoside (OG) solution that is well above the critical micelle concentration. The peptide/OG solution was then added to the lipid vesicle solution, at which point the OG concentration drops below the critical micelle concentration of 7.3 mg/mL at room temperature (21). The mixed solution was shaken for 2 h and dialyzed for three days at room temperature with six buffer changes to remove the detergent. The LW-M2TM sample was reconstituted in the VM+ membrane, whereas the GHW-M2TM sample was reconstituted in the VM membrane. The peptide/lipid molar ratio was 1:15 for all samples. The dialyzed proteoliposomes solutions were centrifuged at 55,000 rpm at 5°C for 4 h to obtain homogeneous membrane pellets, which were spun into 4 mm MAS rotors for solid-state NMR experiments.

## Solid-state NMR experiments

All solid-state NMR (SSNMR) experiments were performed on a Bruker DSX-400 MHz (9.4 T) spectrometer (Bruker Biospin Billerica, MA) using two 4-mm MAS probes tuned to <sup>1</sup>H/<sup>13</sup>C/<sup>15</sup>N and <sup>1</sup>H/<sup>19</sup>F frequencies. Typical radio frequency field strengths were 50 kHz for <sup>13</sup>C, 42 kHz for <sup>15</sup>N, 50 kHz for <sup>19</sup>F, and 62–83 kHz for <sup>1</sup>H. <sup>13</sup>C chemical shifts were referenced to the  $\alpha$ -Gly carbonyl at 176.465 ppm on the tetramethylsilane scale, whereas <sup>15</sup>N chemical shifts were referenced to the <sup>15</sup>N signal of N-acetylvaline at 122.0 ppm on the liquid ammonia scale. <sup>19</sup>F chemical shifts were referenced to the <sup>19</sup>F signal of Teflon at –122.0 ppm.

One-dimensional (1D) <sup>13</sup>C cross-polarization spectra were measured under 7 kHz MAS between 243 K and 303 K. One-dimensional <sup>13</sup>C double-quantum-filtered (DQF) spectra were measured at 303 K under 7 kHz MAS. Two-dimensional (2D) DQF <sup>13</sup>C-<sup>13</sup>C correlation spectra were measured at 273 K under 7 kHz MAS. To determine motional order parameters, we measured <sup>13</sup>C-<sup>1</sup>H dipolar couplings using the dipolar chemical-shift correlation experiment (DIPSHIFT) under 4.4 kHz MAS at 303 K. <sup>1</sup>H homonuclear decoupling was achieved using the MREV-8 sequence with a 90° pulse length of 3.5  $\mu$ s. An MREV-8 scaling factor of 0.47 and a rigid-limit coupling of 22.7 kHz were used to calculate the Trp<sup>41</sup> order parameters. C $\epsilon$ 1-N $\epsilon$ 1 and C $\delta$ 1-N $\epsilon$ 1 dipolar couplings were measured using the rotational-echo double-resonance (REDOR) experiment (22) under 7 kHz MAS at 303 K. To calculate the C-N dipolar order parameter, a rigid-limit coupling of 1.15 kHz was used, which was verified on amino acid tryptophan.

A <sup>13</sup>C-<sup>19</sup>F REDOR experiment was used to measure <sup>13</sup>C-<sup>19</sup>F distances between <sup>13</sup>C-labeled His<sup>37</sup> and 5-<sup>19</sup>F-Trp<sup>41</sup> in the GHW-M2TM samples at pH 8.5 and 4.5. The REDOR pulse sequence utilized composite 90°225°315° <sup>19</sup>F pulses to achieve broadband inversion of the <sup>19</sup>F polarization (23). A soft Gaussian <sup>13</sup>C 180° pulse was applied in the middle of the REDOR period to refocus the <sup>13</sup>C chemical shift and the <sup>13</sup>C-<sup>13</sup>C scalar coupling in the uniformly <sup>13</sup>C-labeled His<sup>37</sup> (24,25). For the low-pH sample, MAS frequencies of 3.0, 3.3, and 6.6 kHz were used to detect the aromatic <sup>13</sup>C signals of His<sup>37</sup> without overlap from the CO sidebands. For the high-pH sample, the REDOR experiment was conducted under

3.3 and 5.0 kHz MAS. All <sup>13</sup>C-<sup>19</sup>F REDOR spectra were measured at 243 K and the mixing times varied from 1.2 to 9.6 ms, with 20,000–70,000 scans of signal averaging per spectrum.

The centerband-only-detection of exchange (CODEX) experiment (26,27) was used to measure interhelical Trp<sup>41</sup>-Trp<sup>41</sup> distances. The experiments were conducted under 8 kHz MAS at ~230 K. Two rotor periods of <sup>19</sup>F  $\pi$ -pulses spaced at every half a rotor period was applied before and after a longitudinal mixing time to recouple the <sup>19</sup>F chemical shift anisotropy. After the second  $\pi$ -pulse train, a second longitudinal mixing time was applied to factor out <sup>19</sup>F T<sub>1</sub> relaxation. Analogous to the REDOR experiments, the CODEX experiments were conducted in a pairwise fashion, with a control (*S*<sub>0</sub>) and dephasing (*S*) experiment, and normalized intensity (*S*<sub>0</sub>/*S*) is fit to obtain distances. CODEX mixing times of 1 ms to 2 s were used.

## Data analysis and simulation

The error bars for the <sup>13</sup>C-<sup>19</sup>F REDOR data points were propagated from the experimental signal/noise ratios. The <sup>13</sup>C-<sup>19</sup>F REDOR *S*/*S*<sub>0</sub> values as a function of mixing time were first simulated using the program SIMPSON (28), assuming two-spin geometry. Best-fit distances were obtained by minimizing the root-mean-square deviations (RMSDs) between the simulated and experimental intensities. After the Trp<sup>41</sup> ( $\chi$ <sub>1</sub>,  $\chi$ <sub>2</sub>) rotamers were determined, we used the SPINEVOLUTION program (29) to conduct model-dependent five-spin (one <sup>13</sup>C and four <sup>19</sup>F spins) simulations for each possible rotamer. PDB files were generated for each Trp<sup>41</sup> rotamer, then the coordinates for each Trp<sup>41</sup> <sup>13</sup>C and <sup>19</sup>F sites were provided to the SPINEVOLUTION program for use in the five-spin simulations.

The <sup>19</sup>F CODEX exchange data were fit using a MATLAB program (The MathWorks, Natick, MA) that employs the exchange-matrix formalism to treat spin diffusion in the four-spin system. The 4 × 4 exchange matrix contains rate constants that are proportional to an overlap integral and the square of the internuclear dipolar couplings. Based on previous model compound results, the overlap integral value is 37  $\mu$ s (10,30) under our experimental conditions. Best-fit distances were obtained by minimizing the RMSD between the calculated and experimental CODEX intensities.

DIPSHIFT curves are simulated using a FORTRAN program. A phenomenological T<sub>2</sub> relaxation time was applied to the best-fit simulated curves to reproduce the observed asymmetry in the time signal.

## Analysis of Trp<sup>41</sup> rotameric conformation

To model the side-chain conformation of Trp<sup>41</sup> from the measured His-Trp and Trp-Trp distances, we first considered the choice of the backbone structure. For the high-pH data, we used the distance-constrained solid-state NMR structure (PDB:2KQT) and the 1.65-Å crystal structure (PDB:3LBW) as backbone structural models, because they have similar helix tilt angles. For the low-pH data, we used the pH 5.3 crystal structure (PDB:3C9J) and the DLPC (dilauroylphosphatidylcholine)-based solid-state NMR structural model (PDB:2KAD) (31,32). These two backbone structures resemble each other in having a helix tilt angle of 35–38°, which is consistent with the helix orientation measured using oriented-membrane solid-state NMR experiments (13,33). The DLPC-based solid-state NMR structure has C<sub>4</sub> symmetry, which simplifies the rotamer analysis, whereas the low-pH crystal structure (PDB:3C9J) has significant asymmetry.

In all distance analyses, the His<sup>37</sup> side chain was fixed to the *tt* rotamer ( $\chi$ <sub>1</sub> =  $\chi$ <sub>2</sub> = 180°) determined by SSNMR and crystallography (6,11). The Trp<sup>41</sup>  $\chi$ <sub>1</sub> and  $\chi$ <sub>2</sub> angles were varied and the His-Trp <sup>13</sup>C-<sup>19</sup>F distances and Trp-Trp intermolecular <sup>19</sup>F-<sup>19</sup>F distances were measured and compared to the experimental data. In a first round of analysis, the Trp<sup>41</sup>  $\chi$ <sub>1</sub> and  $\chi$ <sub>2</sub> angles were manually varied in 30° steps in the program CHIMERA (34) to obtain a coarse-grained map of the possible Trp<sup>41</sup> rotamers that agree with the experimental data. These results were then refined in a second round of analysis, where the software YASARA (35) was used to tabulate the

$^{13}\text{C}$ - $^{19}\text{F}$  and  $^{19}\text{F}$ - $^{19}\text{F}$  distances in  $5^\circ$  steps of  $\chi_1$  and  $\chi_2$ . The best fit was determined by calculating the RMSDs between the model-free two-spin best-fit distances for the experimental data and the model-dependent distances. For the latter, out of four possible values for each type of distance, only the shortest distance was used to compare with the experimental result in order to simplify the analysis. For the high-pH sample, the RMSD was the sum of the C $\alpha$ -F, C $\gamma$ -F, C $\epsilon$ 1-F, and F-F distance RMSDs. For the low-pH sample, the C $\delta$ 2-F distance was also included in the RMSD analysis. The rotamers with the minimum RMSD were then checked in CHIMERA for obvious steric clashes. For the best-fit Trp<sup>41</sup> rotamers without steric conflict, we extracted the shortest  $^{13}\text{C}$ - $^{19}\text{F}$  distances for two-spin SIMPSON simulations of the data, and all four distances for five-spin SPINEVOLUTION simulations. These model-specific simulations were compared with the experimental REDOR and CODEX data to check for agreement.

### Calculation of motionally averaged dipolar couplings in the Trp<sup>41</sup> side chain

The motional amplitudes around the C $\alpha$ -C $\beta$  and C $\beta$ -C $\gamma$  bonds of Trp<sup>41</sup> were reflected in the motionally averaged C-H and C-N dipolar couplings, i.e., order parameters. To constrain the motional geometry, we calculated the order parameters of the indole ring using a Gaussian biaxial fluctuation model (36), where the indole is rotated around the C $\alpha$ -C $\beta$  and C $\beta$ -C $\gamma$  bonds by  $\phi_1$  and  $\phi_2$ , respectively. The distribution of  $\phi_1$  and  $\phi_2$  was a normalized Gaussian function  $g_1$  and  $g_2$  with a standard deviation of  $\sigma_1$  and  $\sigma_2$ , with a cutoff at  $2\sigma_n$ . The most probable rotation angle  $\phi_n$ , which corresponds to the center of the Gaussian, was the equilibrium torsion angle  $\chi_n$ , determined from the  $^{13}\text{C}$ - $^{19}\text{F}$  and  $^{19}\text{F}$ - $^{19}\text{F}$  distance measurements. The two torsional rotations were assumed to be independent, and all covalent bond angles were held fixed.

The C $\beta$ -C $\gamma$  axis was rotated by a certain angle  $\phi_{1,n}$ , around the C $\alpha$ -C $\beta$  bond, then the C-H dipolar tensor in the indole ring was rotated around the C $\beta$ -C $\gamma$  axis by  $\phi_{2,k}$ . The motionally averaged dipolar tensor  $\overline{\overline{D}}(\phi_{1,n}, \phi_{2,k})$  was calculated as the weighted average of the individual rotated tensors ( $3 \times 3$  matrices) for systematically varied  $\phi_{1,n}$  and  $\phi_{2,k}$  values, where the weighting function is the product of the normalized Gaussian distributions:

$$\overline{\overline{D}}(\sigma_1, \sigma_2) = \sum_k \sum_n \overline{\overline{D}}(\phi_{1,n}, \phi_{2,k}) g_1(\phi_{1,n}, \sigma_1) g_2(\phi_{2,k}, \sigma_2).$$

The principal values  $\overline{\overline{D}}_x$ ,  $\overline{\overline{D}}_y$ ,  $\overline{\overline{D}}_z$  of the traceless average tensor  $\overline{\overline{D}}$ , ordered such that  $\overline{\overline{D}}_z$  has the largest magnitude and  $\overline{\overline{D}}_y$  the smallest, give the motionally averaged dipolar coupling constant  $\overline{\overline{d}} = \overline{\overline{D}}_z$ . The asymmetry parameter of the averaged coupling tensor is  $\overline{\overline{\eta}} = (\overline{\overline{D}}_y - \overline{\overline{D}}_x) / \overline{\overline{D}}_z$ . The calculated  $\overline{\overline{d}}$  was converted to the order parameter as  $S_{\text{CH}} = \overline{\overline{d}} / d$ , and then compared with the measured  $S_{\text{CH}}$  from the DIPSHIFT experiments. To determine the values of  $\sigma_1$  and  $\sigma_2$  that are compatible with all measured order parameters,  $S_{\text{CH}}$  as a function of  $\sigma_1$  and  $\sigma_2$  for several indole bonds were superimposed, and the regions consistent with the experimental values were highlighted.

## RESULTS AND DISCUSSION

### Conformation of Trp<sup>41</sup>

To determine the side-chain conformation of Trp<sup>41</sup> and its dependence on pH, we measured the Trp<sup>41</sup>  $^{13}\text{C}$  and  $^{15}\text{N}$  chemical shifts using 2D  $^{13}\text{C}$ - $^{13}\text{C}$  and  $^{15}\text{N}$ - $^{13}\text{C}$  correlation experiments. Fig. 2 shows representative 1D and 2D spectra of LW-M2TM. The 1D  $^{13}\text{C}$  spectra of M2TM show similar  $^{13}\text{C}$  intensity patterns at high and low pH. No significant intensity changes were observed between 303 and 243 K, consistent with the previously reported immobilization of

M2TM by the cholesterol-rich virus-mimetic membranes (19,20). The C $\alpha$  and C $\beta$  chemical shifts of L40 and W41 are generally consistent with the  $\alpha$ -helical secondary structure, as expected for this four-helix bundle. However, the L40 C $\alpha$  and C $\beta$  chemical shifts change to more ideal  $\alpha$ -helical values at low pH (larger C $\alpha$  and smaller C $\beta$  chemical shifts), consistent with previous reports that the helix becomes straighter and more tilted at low pH due to charge repulsion at His<sup>37</sup> (32).

Full assignment of the indole  $^{13}\text{C}$  and  $^{15}\text{N}$  chemical shifts were obtained from 2D  $^{13}\text{C}$ - $^{13}\text{C}$  DQF correlation spectra and  $^{15}\text{N}$ - $^{13}\text{C}$  correlation spectra (Fig. 2, *c* and *d*). In these spectra, only a single chemical shift was observed for each site, with an average  $^{13}\text{C}$  line-width of 1.8 ppm. This contrasts with the peak doubling reported for the longer M2 construct that contains both the TM and cytoplasmic helices (37,38), for which chemical shift differences as large as 2.7 ppm were detected, which is larger than the resolution limit of our spectra. The chemical shift difference for the peak-doubled longer M2 construct is the largest at backbone C $\alpha$  (about 2 ppm), which strongly suggests that the cytoplasmic helix affects the backbone conformation of the TM domain (37,38). This effect is consistent with the recent report that the cytoplasmic helix has the ability to cause the formation of high-curvature membrane domains, which shifts the conformational equilibrium of the TM segment to a form that is incompetent for binding the antiviral drug amantadine (19,39). The absence of such peak doubling for the TM construct used here indicates that the TM segment adopts a single conformation in the absence of the cytoplasmic helix. Based on all available experimental evidence so far (6,19,32), this conformation is sensitive to both pH and drug and is thus functionally relevant.

Further information about the local environment of Trp<sup>41</sup> can be gleaned by comparing the  $^{13}\text{C}$  and  $^{15}\text{N}$  chemical shifts between pH 8.5 and pH 4.5 and between the short and long M2 constructs at high pH (Fig. 2 *e*). For the TM construct, most side-chain atoms exhibit similar (<0.5 ppm) chemical shifts at high and low pH, with the exception of C $\delta$ 1 and C $\zeta$ 2, which also show nonnegligible chemical shift differences between the short and long M2 constructs (Fig. 2 *e*). For C $\alpha$  and C $\beta$  chemical shifts, which are sensitive to the backbone conformation, the long-peptide chemical shifts are closer to the short peptide's low-pH chemical shifts. This phenomenon can be understood. The presence of the cytoplasmic helix is known to moderately increase proton conduction (40), which implies that the channel may adopt the acid-activated conformation more readily in the presence of the cytoplasmic helix. The M2(22–62) chemical shifts were also measured at slightly lower pH (pH 7.5) than the high-pH sample here, thus a higher percentage of tetramers should exist in the partially charged states for proton conduction. Finally, the longer M2 construct was studied in the more fluid membranes of DOPC/DOPE (dioleoylphosphatidyl-choline/dioleoylphosphatidyl-ethanolamine) in one

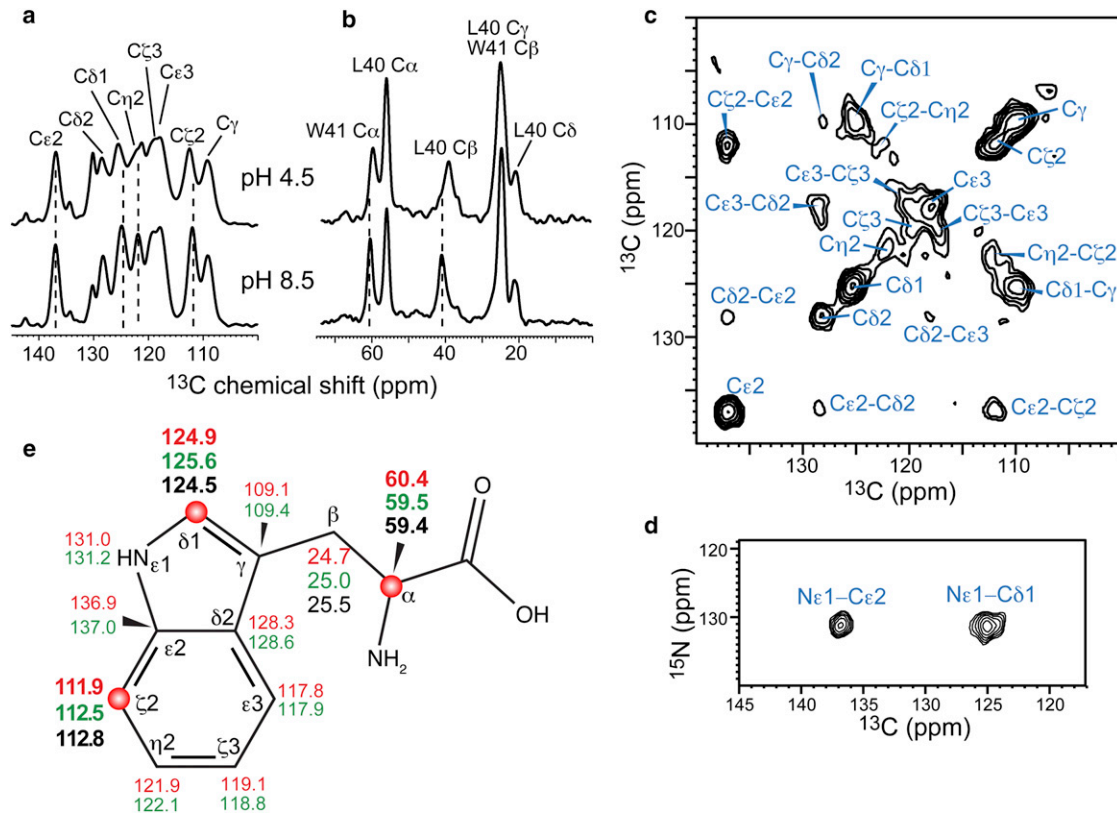


FIGURE 2 Trp<sup>41</sup> chemical shifts at pH 4.5 and 8.5 in LW-M2TM bound to the VM+ membrane. (a) Aromatic region of the 1D <sup>13</sup>C cross-polarization spectra at pH 4.5 and 8.5. (b) Aliphatic region of the 1D <sup>13</sup>C DQF spectra at the two pH conditions. The lipid peaks were suppressed by the double-quantum filter. Note the chemical shift changes of Trp<sup>41</sup> and Leu<sup>40</sup> Cα and Cβ peaks, indicating pH-induced small conformation changes of the helix backbone. (c) 2D <sup>13</sup>C-<sup>13</sup>C DQF spectrum of LW-M2TM at pH 8.5. (d) 2D <sup>15</sup>N-<sup>13</sup>C correlation spectrum of the peptide at high pH. (e) Summary of Trp<sup>41</sup> <sup>13</sup>C and <sup>15</sup>N chemical shifts at high pH (red) and low pH (green). (Black) High-pH chemical shifts of M2(22–62) in DOPC/DOPE bilayers (38) for sites that have >0.5 ppm chemical shift difference from the M2TM values. (Bold) Chemical shifts that differ by >0.5 ppm between high and low pH. All <sup>13</sup>C chemical shifts are reported on the tetramethylsilane scale.

case (38) and DPhPC (diphytanoylphosphatidylcholine) membrane in another (37), which should facilitate the conformational motion that is necessary for the TM helix to adopt the low-pH conformation.

### His<sup>37</sup>-Trp<sup>41</sup> and Trp<sup>41</sup>-Trp<sup>41</sup> distances

His<sup>37</sup>-Trp<sup>41</sup> aromatic interactions have been implicated in channel gating at low pH based on resonance Raman data (17). Here we directly measured the distances between these two residues using <sup>13</sup>C-labeled His<sup>37</sup> and 5-<sup>19</sup>F-labeled Trp<sup>41</sup> (Fig. 3 a). The latter corresponds to the Hζ3 position of the indole ring. The high gyromagnetic ratio of the <sup>19</sup>F spin allows <sup>13</sup>C-<sup>19</sup>F distances to be measured up to ~8 Å (~55 Hz) (23,41). We measured the <sup>13</sup>C-<sup>19</sup>F distances using a variant of the REDOR experiment, where a selective <sup>13</sup>C π-pulse was applied in the middle of the REDOR period to suppress one-bond <sup>13</sup>C-<sup>13</sup>C J-coupling and lengthen the effective <sup>13</sup>C T<sub>2</sub> (24,25). Fig. 3, b and c, shows representative REDOR spectra, where the His<sup>37</sup> Cγ, Cε1, and Cδ2 signals, which are sensitive to pH, are assigned according to published 2D spectra (6). Several MAS frequencies

were used in these experiments to avoid resonance overlap between the carbonyl sidebands and the aromatic carbons of interest. The largest intensity differences between the control (S<sub>0</sub>) and dephased (S) REDOR spectra were observed for Cγ and Cδ2 of the low-pH sample, which showed S/S<sub>0</sub> values as low as 0.3 by ~8 ms. The high-pH peptide shows comparatively less REDOR dephasing, indicating longer distances between His<sup>37</sup> and Trp<sup>41</sup>. The difference is the largest for Cγ (Fig. 3 d), whose dephasing corresponds to a two-spin Cγ-F distance of 8.4 Å at pH 8.5 but 6.2 Å at pH 4.5. For Cδ2, only low-pH data could be obtained with sufficient sensitivity, and the REDOR dephasing was fast, corresponding to a short two-spin distance of 6.0 Å.

Complementing the His<sup>37</sup>-Trp<sup>41</sup> <sup>13</sup>C-<sup>19</sup>F distances, we also measured the <sup>19</sup>F-<sup>19</sup>F distances using the <sup>19</sup>F CODEX experiment (see Fig. S1 in the Supporting Material). We have previously measured these distances in DMPC (dimyristoylphosphatidylcholine)-bound M2TM, where the peptide was reconstituted into the membrane using a different protocol (10). Under those conditions, the nearest-neighbor distance between the <sup>19</sup>F spins was 11 ± 1 Å at

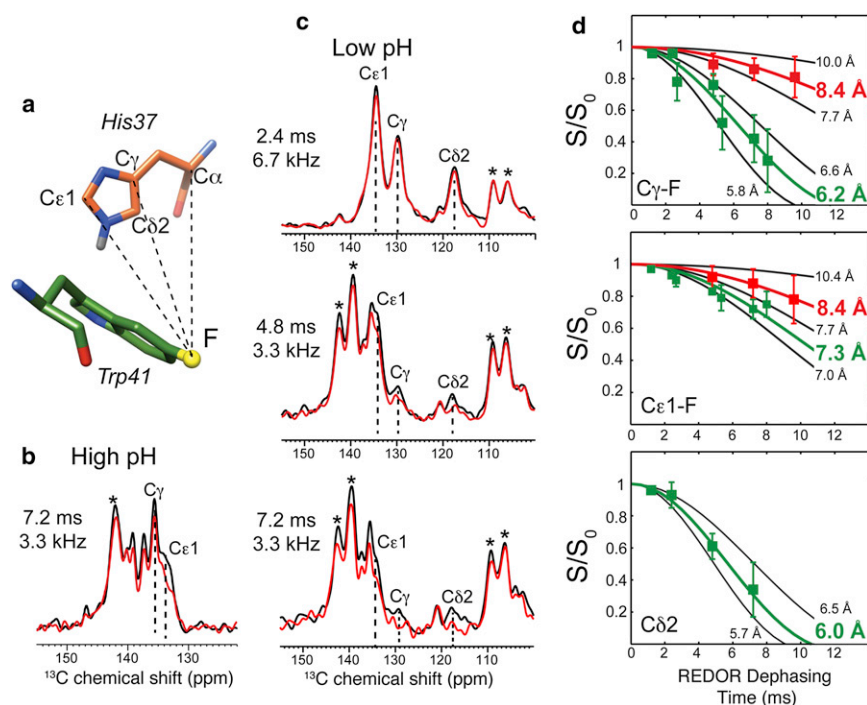


**FIGURE 3**  $^{13}\text{C}$ - $^{19}\text{F}$  REDOR distance measurements of  $^{13}\text{C}$ -labeled His<sup>37</sup> and  $5\text{-}^{19}\text{F}$ -labeled Trp<sup>41</sup> in VM bound M2TM. (a) Approximate spatial arrangement of His<sup>37</sup> of one helix and Trp<sup>41</sup> of the neighboring helix. (b) Representative  $^{13}\text{C}$ -detected  $^{19}\text{F}$ -dephased REDOR control ( $S_0$ , black) and dephased ( $S$ , red) spectra of the peptide at pH 8.5. The spectra were measured at 243 K under 3.3 kHz MAS. (c) Representative REDOR spectra of the peptide at pH 4.5. The spectra were measured under 3.0, 3.3, and 6.7 kHz MAS in order to detect all His<sup>37</sup> aromatic  $^{13}\text{C}$  signals without overlap from the carbonyl sidebands (asterisks). (d)  $^{13}\text{C}$ - $^{19}\text{F}$  REDOR  $S/S_0$  intensity as a function of mixing time for the high-pH (red) and low-pH (green) peptides. De novo two-spin simulations are shown. Best-fit distances are highlighted for the high-pH data (red) and the low-pH data (green).

both high and low pH. For the virus-mimetic membrane samples prepared by detergent dialysis, the CODEX dephasing curves show detectable differences between high and low pH: the best-fit nearest-neighbor distance is 11.3 Å at high pH and 12.4 Å at low pH, indicating that the inter-Trp separation is enlarged at low pH. This is consistent with most available experimental evidence showing that the C-terminal region of the four-helix bundle is expanded at low pH (12).

### pH-dependent Trp<sup>41</sup> rotameric structure and His<sup>37</sup>-Trp<sup>41</sup> contact

These  $^{13}\text{C}$ - $^{19}\text{F}$  and  $^{19}\text{F}$ - $^{19}\text{F}$  distances, together with the known backbone structure of M2TM (42) and the known His<sup>37</sup> side-chain conformation (6), allowed us to constrain the Trp<sup>41</sup> side-chain conformation. Two PDB structures were used for each pH condition to assess the influence of the backbone conformation on the Trp<sup>41</sup> rotamer determination. Interresidue distances were extracted as a function of Trp<sup>41</sup>  $\chi_1$  and  $\chi_2$  angles to compare with the measured  $^{13}\text{C}$ - $^{19}\text{F}$  and  $^{19}\text{F}$ - $^{19}\text{F}$  distances. The two high-pH models (PDB:2KQT and PDB:3LBW) yielded a consistent best-fit rotamer of  $(-175^\circ, +120^\circ)$  (Fig. 4), indicating that the rotamer is  $\sim t90$ . In contrast, the two low-pH structures did not give a single consensus rotamer. The solid-state NMR backbone structure (PDB:2KAD) gave a best-fit Trp<sup>41</sup> rotamer of  $(-155^\circ, 135^\circ)$  whereas the low-pH crystal structure (PDB:3C9J) gave two possible Trp<sup>41</sup> rotamers:  $(-115^\circ, 45^\circ)$  and  $(-145^\circ, -125^\circ)$  when solutions with steric clashes were ruled out. Because the PDB: 3C9J backbone shows considerable asymmetry, and it is energetically more costly

for Trp<sup>41</sup> to undergo a large-angle conformational change than a small-angle change between high and low pH, we favor the  $(-155^\circ, 135^\circ)$  rotamer as the low-pH Trp<sup>41</sup> conformation. The overall similarity of the  $\chi_2$  angle at high and low pH is consistent with the Raman data (17), whereas the *trans*- $\chi_1$  angle is consistent with the previously measured His<sup>37</sup>  $\text{N}\epsilon_2$ -Trp<sup>41</sup>  $\text{C}\gamma$  distance (13). Other rotamer minima seen in Fig. 4 can be ruled out based on steric conflicts. For example, multiple rotamer minima in PDB:3C9J have steric clashes with either the helix backbone or other side chains in the HxxxW segment (see Fig. S2, a and b). The  $(-90^\circ, 180^\circ)$  rotamer in PDB:3LBW and PDB:2KAD causes steric clashes among the four Trp side chains (see Fig. S2 c). The  $(95^\circ, -125^\circ)$  rotamer in PDB:3LBW and PDB:2KQT is rarely populated in the protein database (43) and is therefore not considered further (see Fig. S2 d).

Fig. 5, a and b, shows model-dependent fits of the  $^{13}\text{C}$ - $^{19}\text{F}$  REDOR and  $^{19}\text{F}$ - $^{19}\text{F}$  CODEX data at high and low pH for the best-fit Trp<sup>41</sup> rotamers. For the  $^{13}\text{C}$ - $^{19}\text{F}$  REDOR data, the five-spin and two-spin simulations both show good agreement with the measured data within experimental uncertainty, indicating that the shortest interhelical distance accounts for the majority of the observed REDOR dephasing.

The high- and low-pH His-Trp side chains are compared in Fig. 5, c and d. At both pH conditions, the Trp<sup>41</sup> side chain broadly adopts the *t90* rotamer, which is consistent with the observed pH sensitivity of the C $\delta$ 1 and C $\zeta$ 2 chemical shifts, because these two carbons of the indole ring face the aqueous pore. In contrast, the *t*-105 rotamer would point C $\delta$ 1 to the lipid (Fig. 1), inconsistent with the pH sensitivity

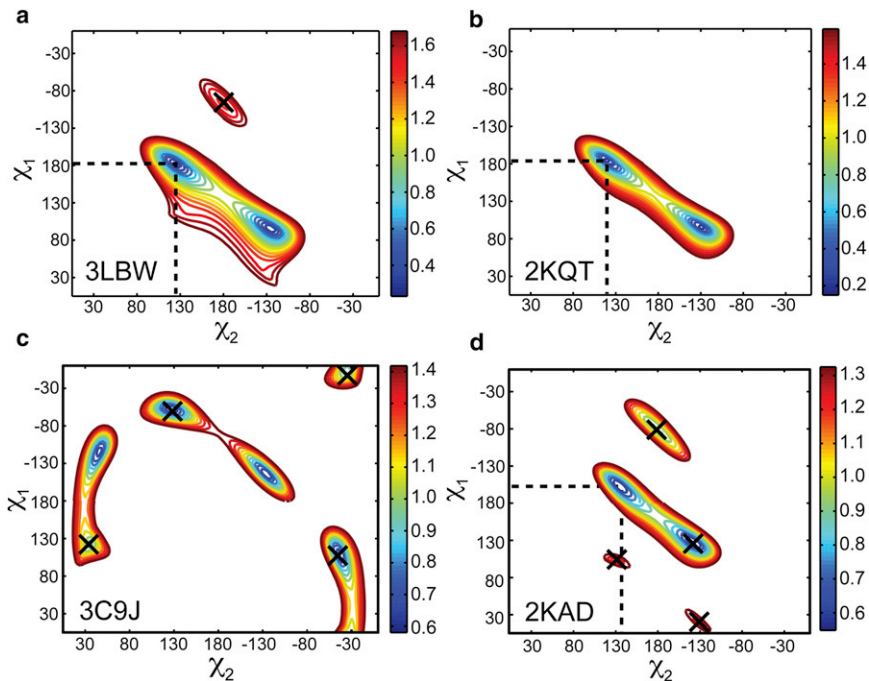


FIGURE 4 Total RMSD between the measured and modeled  $C\alpha$ -F,  $C\gamma$ -F,  $C\epsilon 1$ -F,  $C\delta 2$ -F, and  $^{19}\text{F}$ - $^{19}\text{F}$  distances as a function of  $\text{Trp}^{41}$  ( $\chi_1$ ,  $\chi_2$ ) torsion angles. Different backbone structure models for M2TM at high (*a* and *b*) and low (*c* and *d*) pH are used for structural modeling. Only the shortest of the four possible distances in the tetramer for each two-spin combination is used to compare with the experimental data. (*a*) PDB:3LBW backbone structure. (*b*) PDB:2KQT backbone structure. (*c*) PDB:3C9J backbone structure. (*d*) PDB:2KAD backbone structure. Between the two high-pH backbone structures, consensus ( $\chi_1$ ,  $\chi_2$ ) results were found at  $(-175^\circ, 120^\circ)$ . For the low-pH state, the best-fit  $\text{Trp}^{41}$  rotamer depends on the backbone structure. For the PDB:2KAD structure (*d*), the best-fit solution is  $(\chi_1, \chi_2) = (-155^\circ, 135^\circ)$ , whereas the PDB:3C9J structure (*c*) shows two rotamer minima without steric conflict. (*Crosses*) Rotamers with steric clashes, which are not considered further (see Fig. S2).

of its chemical shift. Under this broad similarity of the  $\text{Trp}^{41}$  rotamer,  $\text{His}^{37}$  and  $\text{Trp}^{41}$  establish closer contact at low pH, due to a downward movement of the imidazole rings as a result of the larger helix tilt angle. The  $15$ – $20^\circ$   $\text{Trp}^{41}$   $\chi_1$  and  $\chi_2$  angle differences between the two pH have a more subtle effect on the aromatic packing: the  $\chi_1$  change (from  $-175^\circ$  at high pH to  $-155^\circ$  at low pH) pushes the indole ring toward the center of the channel, while the  $\chi_2$  change (from  $120^\circ$  at high pH to  $135^\circ$  at low pH) moves the  $C\eta 2/C\zeta 3$  end of the indole toward the C-terminus. These counterdirectional  $\chi_1$  and  $\chi_2$  changes may serve to avoid steric clashes with the side chains of  $\text{Leu}^{38}$  and  $\text{Ile}^{42}$  while still allowing the indole face to be exposed to  $\text{His}^{37}$ . The closer contact between the imidazole and indole rings of two neighboring helices at low pH creates stronger aromatic interactions, consistent with the Raman spectral changes (17).

### Dynamics of the $\text{Trp}^{41}$ side chain

To investigate whether the  $\text{Trp}^{41}$  side chain is dynamic to affect proton gating and interaction with  $\text{His}^{37}$ , we measured the order parameters of several indole  $^{13}\text{C}$ - $^1\text{H}$  and  $^{13}\text{C}$ - $^{15}\text{N}$  bonds at high temperature. Fig. 6 shows representative  $^{13}\text{C}$ - $^1\text{H}$  and  $^{13}\text{C}$ - $^{15}\text{N}$  dipolar coupling data obtained at 303 K. The  $^{13}\text{C}$ - $^1\text{H}$  dipolar couplings were measured using the 2D DIPSHIFT experiment whereas the  $^{13}\text{C}$ - $^{15}\text{N}$  dipolar couplings were measured using REDOR. We found order parameters of  $0.7$ – $0.9$  for the indole bonds (with uncertainty of  $0.05$ ), with the lowest bond order parameters along the  $C\zeta 2$ - $C\epsilon 3$  axis. pH change caused the largest difference in the order parameters of the  $C\delta 1$ -H and  $C\zeta 3$ -H bonds, with

the low-pH sample showing smaller  $S_{\text{CH}}$  values or larger-amplitude dynamics.

Qualitatively, the relatively large order parameters ( $>0.7$ ) indicate that the motional amplitude of the indole ring is small at both pH conditions. To determine the motional geometry, we first considered simple two-site jump motions around either the  $C\beta$ - $C\gamma$  bond ( $\chi_2$ ) or the  $C\alpha$ - $C\beta$  bond ( $\chi_1$ ). The indole bonds have fixed orientations from the  $C\beta$ - $C\gamma$  axis but variable angles from the  $C\alpha$ - $C\beta$  axis depending on the  $\chi_2$  angle. The equilibrium ( $\chi_1$ ,  $\chi_2$ ) angles are known from the above His-Trp distance measurements:  $(-175^\circ, 120^\circ)$  at high pH and  $(-155^\circ, 135^\circ)$  at low pH. Thus, the indole bond orientations relative to the  $C\alpha$ - $C\beta$  and  $C\beta$ - $C\gamma$  axes are determined by the equilibrium conformation and the jump angle. We calculated the average dipolar couplings as a function of jump angle for the various indole bonds, as shown before for  $\text{His}^{37}$  (6), and did not find any jump angle that simultaneously satisfied all the measured order parameters. This indicates that the indole ring does not undergo a simple two-site jump motion.

This prompted us to consider a more general motional model, which is Gaussian fluctuation of the indole ring around both the  $C\alpha$ - $C\beta$  and  $C\beta$ - $C\gamma$  bonds with Gaussian widths  $\sigma_1$  and  $\sigma_2$ . Successive rotations around the  $C\alpha$ - $C\beta$  and  $C\beta$ - $C\gamma$  bonds change the orientations of the indole bonds and the associated dipolar couplings. The average dipolar coupling tensors were obtained as a function of the standard deviation,  $\sigma_1$  and  $\sigma_2$ , of the Gaussian functions. The principal values of the average tensor yielded the order parameter and average asymmetry parameter. Fig. 6, *e* and *f*, shows the  $(\sigma_1, \sigma_2)$  values for the calculated

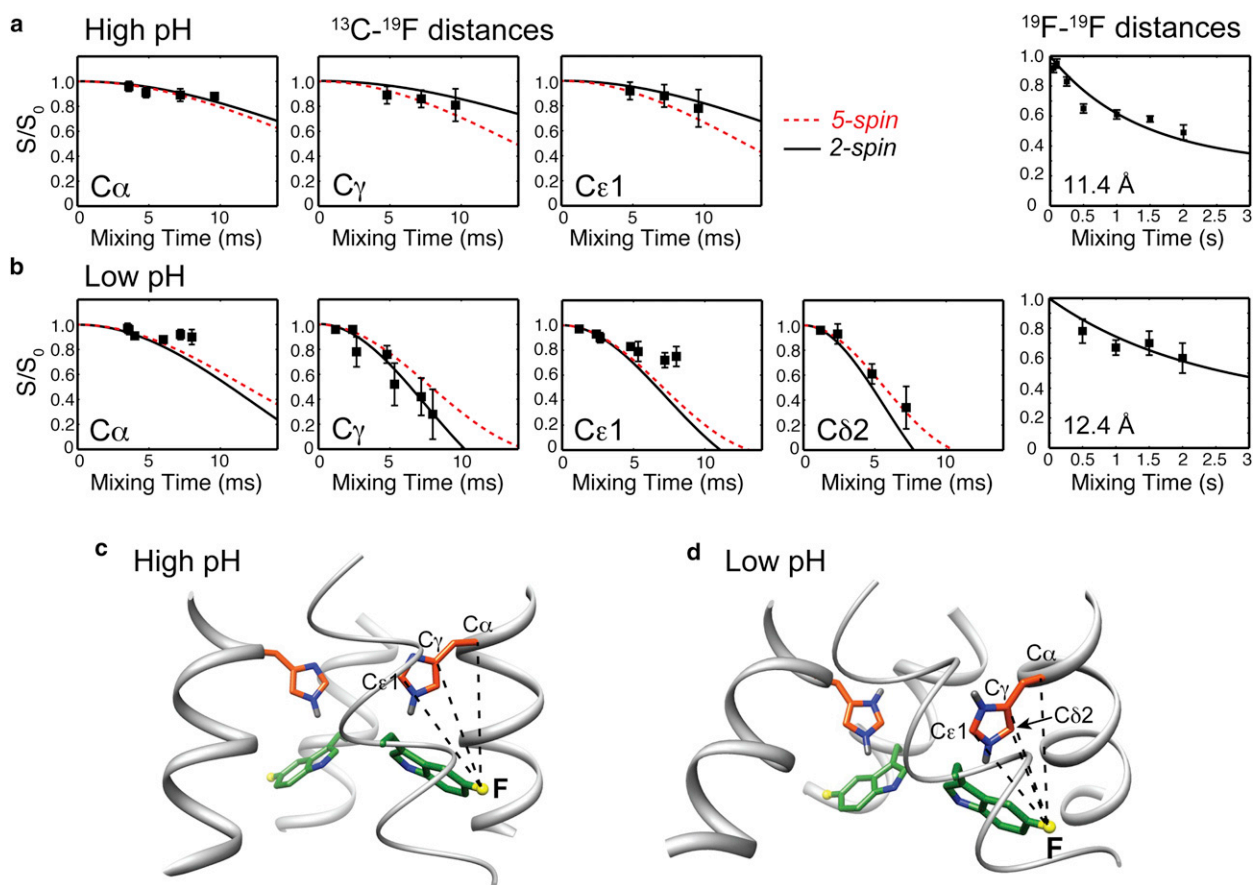


FIGURE 5 His<sup>37</sup>-Trp<sup>41</sup> contacts and Trp<sup>41</sup> side-chain conformation at high and low pH. (a) Best fits of the <sup>13</sup>C-<sup>19</sup>F REDOR and <sup>19</sup>F-<sup>19</sup>F CODEX data at high pH, using PDB:2KQT for the backbone structure and a Trp<sup>41</sup> rotamer of  $\chi_1 = -175^\circ$  and  $\chi_2 = +120^\circ$ . (Red and black curves) Model-dependent five-spin and two-spin best-fit simulations. (b) Best fits of the <sup>13</sup>C-<sup>19</sup>F REDOR and <sup>19</sup>F-<sup>19</sup>F CODEX data at low pH, using PDB:2KAD as the backbone structure and a Trp<sup>41</sup> rotamer of  $\chi_1 = -155^\circ$  and  $\chi_2 = +135^\circ$ . (c) His-Trp region of the high-pH structure (PDB:2KQT), with Trp<sup>41</sup> ( $\chi_1, \chi_2$ ) angles of  $(-175^\circ, 120^\circ)$ . (d) His-Trp region of the low-pH structure (PDB:2KAD), where the Trp<sup>41</sup> rotamer is  $(-155^\circ, 135^\circ)$ . (Dashed lines) Relevant His-Trp <sup>13</sup>C-<sup>19</sup>F distances. At low pH, the imidazole and indole rings approach each other more closely, due to the combined effect of the helix backbone orientation change and Trp<sup>41</sup> ( $\chi_1, \chi_2$ ) changes.

C $\delta$ 1-H $\delta$ 1, C $\zeta$ 2-H $\zeta$ 2, C $\epsilon$ 3-H $\epsilon$ 3, and C $\zeta$ 3-H $\zeta$ 3 order parameters that agree with the measured  $S_{CH}$  values within experimental uncertainty. For the low-pH data, the Gaussian widths that agree with all measured  $S_{CH}$  values are approximately  $\sigma_1 = 30^\circ$  and  $\sigma_2 = 15^\circ$ , indicating that the indole undergoes small-angle fluctuations around both the  $\chi_1$  and  $\chi_2$  bonds. In contrast, at high pH, the larger  $S_{CH}$  for C $\delta$ 1-H and C $\zeta$ 3-H bonds indicate a clear change in the motional geometry, with negligible  $\chi_2$  changes. The remaining  $\chi_1$  torsional motion has a  $\sigma_1$  of  $25^\circ$ . At both pH, the calculations show that the motionally averaged asymmetry parameters do not deviate significantly from uniaxiality (see Fig. S3), thus validating the uniaxial approximation in the order parameter extraction from the experimental data.

Fig. 7 depicts the equilibrium Trp<sup>41</sup> rotameric conformation at high and low pH as well as their dynamic changes. To indicate the range of excursion of the indole ring, we show two limiting rotamers that are one standard deviation ( $\sigma$ )

away from the equilibrium  $\chi_1$  and  $\chi_2$  angles. It can be seen that at acidic pH, not only is the average position of the indole ring closer to the imidazolium compared to high pH, but the  $\chi_1$  and  $\chi_2$  motions further appose the indole to His<sup>37</sup>. As a result, at low pH, the indole alternates between very strong and very weak cation- $\pi$  interactions with the imidazolium during its reorientational motion (44). To give a quantitative estimate of the His<sup>37</sup>-Trp<sup>41</sup> proximity, we calculated the distances of His<sup>37</sup> N $\epsilon$ 2 to the center of the six-membered benzene ring and the center of the five-membered pyrrole ring. For the equilibrium low-pH Trp<sup>41</sup> rotamer of  $(-155^\circ, 135^\circ)$ , N $\epsilon$ 2 is 4.3 Å from the center of the benzene ring and 3.0 Å from the pyrrole ring (Table 2). Due to the torsional fluctuation, the closest approach of indole to the imidazolium has distances of 3.5 Å and 2.5 Å, whereas the remote position of the indole shows a N $\epsilon$ 2-benzene distance of 5.3 Å and an N $\epsilon$ 2-pyrrole distance of 3.6 Å. For comparison, at high pH, the His-Trp distances for the equilibrium Trp<sup>41</sup> conformation are longer,

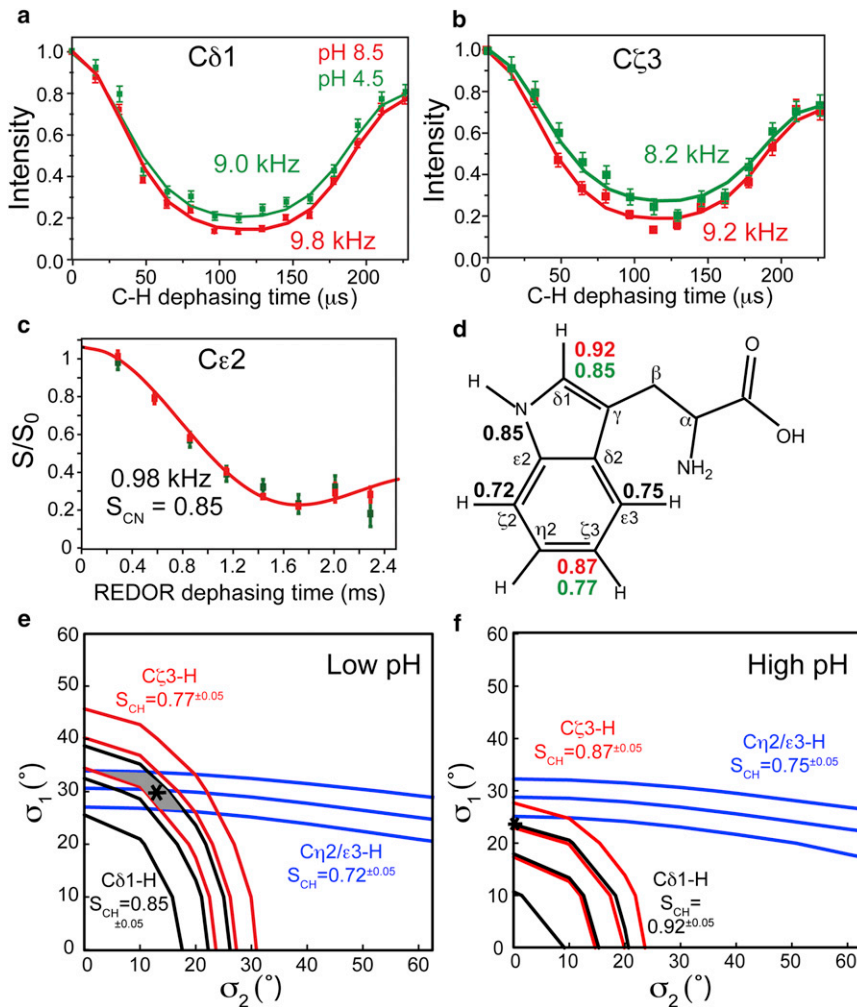


FIGURE 6 Trp<sup>41</sup> side-chain dynamics at high pH (red) and low pH (green) in VM+ membranes at 303 K. (a and b) Representative <sup>13</sup>C-<sup>1</sup>H DIPSHIFT curves for (a) Cδ1-H and (b) Cζ3-H couplings. (c) Cε2-Ne1 REDOR dephasing curve. (d) Summary of all dipolar order parameters of the indole ring at high and low pH. Cδ1-H and Cζ3-H bonds show different order parameters between high (red) and low (green) pH. Most order parameters have an experimental uncertainty of ±0.05. (e) Calculated order parameters as a function of the standard deviations ( $\sigma$ ) of the Gaussian fluctuations around the C $\alpha$ -C $\beta$  and C $\beta$ -C $\gamma$  bonds. Only values that agree with the measured low-pH  $S_{CH}$  are shown. Small-amplitude Gaussian fluctuations with  $\sigma_1 \approx 30^\circ$  and  $\sigma_2 \approx 15^\circ$  (shaded area) agree with all measured order parameters. (f) Calculated order parameters that agree with the high-pH  $S_{CH}$  values. Only torsional motion around the  $\chi_1$  axis is compatible with the experimental data, with  $\sigma_1 \approx 25^\circ$  (indicated by a star).

5.4 Å and 3.7 Å, respectively, comparable to the largest separation at low pH, and the Trp<sup>41</sup> motional range is too small to make a significant difference (Table 2).

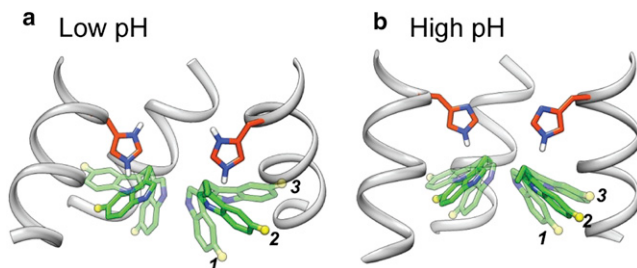


FIGURE 7 Trp<sup>41</sup> conformational dynamics and aromatic interaction with His<sup>37</sup>. (a) Low-pH scenario. The measured equilibrium ( $\chi_1, \chi_2$ ) rotamer of ( $-155^\circ, 135^\circ$ ) is shown as position 2, together with two limiting rotamers based on the measured order parameters. The ( $-125^\circ, 150^\circ$ ) rotamer (position 3) is closer to His<sup>37</sup> whereas the ( $175^\circ, 120^\circ$ ) rotamer (position 1) is further away from His<sup>37</sup>. These angles were chosen to be one standard deviation ( $30^\circ$  for  $\sigma_1$  and  $15^\circ$  for  $\sigma_2$ ) from the average angle. (b) High-pH scenario. The equilibrium rotamer is ( $-175^\circ, 120^\circ$ ) (position 2), and the limiting rotamers are ( $-150^\circ, 120^\circ$ ) (position 1) and ( $160^\circ, 120^\circ$ ) (position 3), based on a  $\sigma_1$  of  $25^\circ$  and no  $\chi_2$  fluctuation.

### Implication of the Trp<sup>41</sup> structure and dynamics to channel gating

The above results provide direct experimental evidence for the closer contact between His<sup>37</sup> and Trp<sup>41</sup> at acidic pH and the existence of the cation- $\pi$  interaction. The closest approach between His<sup>37</sup> Ne2 and the indole face is 2.5 Å, which is shorter than the reported distance range of 3.5–4.0 Å between cationic amino-acid side chains such as

TABLE 2 Trp<sup>41</sup>-His<sup>37</sup> distances as a function of pH and rotameric dynamics

pH	Indole position	Trp <sup>41</sup> ( $\chi_1, \chi_2$ )	Ne2-benzene (Å)	Ne2-pyrrole (Å)
Low	Position 3	( $-125^\circ, 150^\circ$ )	3.5	2.5
	Equilibrium	( $-155^\circ, 135^\circ$ )	4.3	3.0
	Position 1	( $175^\circ, 120^\circ$ )	5.3	3.6
High	Position 3	( $160^\circ, 120^\circ$ )	5.3	3.6
	Equilibrium	( $-175^\circ, 120^\circ$ )	5.4	3.7
	Position 1	( $-150^\circ, 120^\circ$ )	5.5	3.8

His<sup>37</sup> Ne2 distances to the center of the six-membered benzene ring and to the midpoint of the Ne1-C $\gamma$  vector of the pyrrole ring are listed. Positions 3 and 1 correspond to those shown in Fig. 7.

Arg and aromatic rings (44) in proteins. This close proximity is achieved by the combined actions of the increased helix tilt angle and the Trp<sup>41</sup> side-chain conformational dynamics. At low pH, the equilibrium conformation of Trp<sup>41</sup> is roughly perpendicular to the His<sup>37</sup> side chain (Fig. 7), suggesting that the His-Trp interaction has a significant hydrogen-bonding component (44). At high pH, the equilibrium position of the indole ring is similar to the furthest position of the indole from the imidazolium at low pH, and the motional amplitude is insufficient to bring the indole closer to His<sup>37</sup>. Therefore, the aromatic interaction is significantly weaker.

We propose that this close contact between His<sup>37</sup> and Trp<sup>41</sup> at low pH is an important reason for the low proton flux of the M2 channel compared to the measured His<sup>37</sup>-water proton-exchange rate. <sup>15</sup>N NMR lineshapes indicated a water-His<sup>37</sup> proton exchange rate of  $4.5 \times 10^5 \text{ s}^{-1}$  between pH 5 and 6 (7). This is at least two orders of magnitude faster than the proton flux of  $10\text{--}10^3$  per second estimated from whole-cell currents and liposome assays (45–47). Therefore, at most only 1% of His-exchanged protons successfully reach the virion. The dynamically fluctuating His-Trp separation at low pH obtained from our experiments suggest that, when the indole approaches the imidazolium ring, the cation- $\pi$  interaction should prevent proton dissociation from His<sup>37</sup> to water, while as the indole moves away from the imidazolium, the protons can be released to water. This concept has been recently proposed based on molecular modeling of the His-Trp dyad (18). Our results provide the first concrete experimental evidence for this dynamic gating model.

In addition to Trp<sup>41</sup>-mediated regulation of the proton flux, other mechanisms can exist to affect the number of protons released to the C-terminus: these include futile exchange between multiple histidines through intervening water molecules (8) and occasional proton release to the N-terminus, although the latter should be much less frequent than proton release to the C-terminus due to the inherent pH gradient in the channel (48).

In a channel with a reverse proton gradient, where the virus interior is acidic but the exterior is neutral, the lack of reverse current has been attributed to the gating function of Trp<sup>41</sup> (9). Although NMR experiments, similar to most other biophysical techniques, cannot easily mimic the pH gradient used in functional assays, our data provide some insight into this inward rectification. The distance-based structural modeling here indicates that the key first event that reduces the His-Trp separation is the backbone orientational change due to His-His charge repulsion. Thus, as long as the protons from the virus interior cannot pass Trp<sup>41</sup> to reach His<sup>37</sup>, no imidazole protonation and charge repulsion can occur, and the helix tilt angle will remain relatively small, corresponding to the situation in Fig. 7 b.

## CONCLUSION

The His-Trp distances, Trp<sup>41</sup> chemical shifts and dynamics measured here provide detailed insights into the aromatic interaction between these two essential functional residues of the M2 proton channel. Our results indicate that the two aromatic side chains are able to approach each other at low pH due to the increased tilt angle of the helix and the microsecond ( $\chi_1$ ,  $\chi_2$ ) torsional fluctuations of the indole ring at low pH. The low-pH side-chain motion periodically enhances and weakens the His<sup>37</sup>-Trp<sup>41</sup> cation- $\pi$  interaction as the indole moves through its trajectory, thus blocking and releasing protons. In contrast, at high pH only  $\chi_1$  motion is present and the average position of the indole is further from the imidazole due to small ( $\chi_1$ ,  $\chi_2$ ) changes. The pH-dependent Trp<sup>41</sup> side-chain dynamics, with amplitudes of  $15\text{--}30^\circ$ , are reminiscent of the small-angle ( $45^\circ$ )  $\chi_2$  change of His<sup>37</sup> that shuttles protons (6,7). Nature seems to have designed the compact functional heart of this ion channel by relying on economical small-angle side-chain conformational dynamics, coupled with backbone orientational changes, to regulate proton conduction and channel gating.

## SUPPORTING MATERIAL

Three figures are available at [http://www.biophysj.org/biophysj/supplemental/S0006-3495\(13\)00326-3](http://www.biophysj.org/biophysj/supplemental/S0006-3495(13)00326-3).

This work is supported by National Institutes of Health grant No. GM088204.

## REFERENCES

- Pinto, L. H., and R. A. Lamb. 2006. The M2 proton channels of influenza A and B viruses. *J. Biol. Chem.* 281:8997–9000.
- Cady, S. D., W. B. Luo, ..., M. Hong. 2009. Structure and function of the influenza A M2 proton channels. *Biochemistry.* 48:7356–7364.
- Hong, M., and W. F. DeGrado. 2012. Structural basis for proton conduction and inhibition by the influenza M2 protein. *Protein Sci.* 21:1620–1633.
- Ciampor, F., D. Cmarko, ..., E. Závodská. 1995. Influenza virus M2 protein and hemagglutinin conformation changes during intracellular transport. *Acta Virol.* 39:171–181.
- Rossman, J. S., X. Jing, ..., R. A. Lamb. 2010. Influenza virus M2 protein mediates ESCRT-independent membrane scission. *Cell.* 142:902–913.
- Hu, F., W. Luo, and M. Hong. 2010. Mechanisms of proton conduction and gating in influenza M2 proton channels from solid-state NMR. *Science.* 330:505–508.
- Hu, F., K. Schmidt-Rohr, and M. Hong. 2012. NMR detection of pH-dependent histidine-water proton exchange reveals the conduction mechanism of a transmembrane proton channel. *J. Am. Chem. Soc.* 134:3703–3713.
- Hong, M., K. J. Fritzsche, and J. K. Williams. 2012. Hydrogen-bonding partner of the proton-conducting histidine in the influenza M2 proton channel revealed from <sup>1</sup>H chemical shifts. *J. Am. Chem. Soc.* 134:14753–14755.

9. Tang, Y., F. Zaitseva, ..., L. H. Pinto. 2002. The gate of the influenza virus M2 proton channel is formed by a single tryptophan residue. *J. Biol. Chem.* 277:39880–39886.
10. Luo, W., R. Mani, and M. Hong. 2007. Sidechain conformation and gating of the M2 transmembrane peptide proton channel of influenza A virus from solid-state NMR. *J. Phys. Chem.* 111:10825–10832.
11. Acharya, A., V. Carnevale, ..., M. L. Klein. 2010. Structure and mechanism of proton transport through the transmembrane tetrameric M2 protein bundle of the influenza A virus. *Proc. Natl. Acad. Sci. USA.* 107:15075–15080.
12. Stouffer, A. L., R. Acharya, ..., W. F. DeGrado. 2008. Structural basis for the function and inhibition of an influenza virus proton channel. *Nature.* 451:596–599.
13. Nishimura, K., S. Kim, ..., T. A. Cross. 2002. The closed state of a H<sup>+</sup> channel helical bundle combining precise orientational and distance restraints from solid state NMR. *Biochemistry.* 41:13170–13177.
14. Schnell, J. R., and J. J. Chou. 2008. Structure and mechanism of the M2 proton channel of influenza A virus. *Nature.* 451:591–595.
15. Pielak, R. M., J. R. Schnell, and J. J. Chou. 2009. Mechanism of drug inhibition and drug resistance of influenza A M2 channel. *Proc. Natl. Acad. Sci. USA.* 106:7379–7384.
16. Witter, R., F. Nozairov, ..., R. Fu. 2008. Solid-state <sup>19</sup>F NMR spectroscopy reveals that Trp<sup>41</sup> participates in the gating mechanism of the M2 proton channel of influenza A virus. *J. Am. Chem. Soc.* 130:918–924.
17. Okada, A., T. Miura, and H. Takeuchi. 2001. Protonation of histidine and histidine-tryptophan interaction in the activation of the M2 ion channel from influenza A virus. *Biochemistry.* 40:6053–6060.
18. Sharma, M., M. Yi, ..., T. A. Cross. 2010. Insight into the mechanism of the influenza A proton channel from a structure in a lipid bilayer. *Science.* 330:509–512.
19. Cady, S. D., T. Wang, and M. Hong. 2011. Membrane-dependent effects of a cytoplasmic helix on the structure and drug binding of the influenza virus M2 protein. *J. Am. Chem. Soc.* 133:11572–11579.
20. Luo, W., S. D. Cady, and M. Hong. 2009. Immobilization of the influenza A M2 transmembrane peptide in virus envelope-mimetic lipid membranes: a solid-state NMR investigation. *Biochemistry.* 48:6361–6368.
21. da Graça Miguel, M., O. Eidelman, ..., A. Walter. 1989. Temperature dependence of the vesicle-micelle transition of egg phosphatidylcholine and octyl glucoside. *Biochemistry.* 28:8921–8928.
22. Gullion, T., and J. Schaefer. 1989. Rotational echo double resonance NMR. *J. Magn. Reson.* 81:196–200.
23. Wi, S., N. Sinha, and M. Hong. 2004. Long-range <sup>1</sup>H-<sup>19</sup>F distance measurement in peptides by solid-state NMR. *J. Am. Chem. Soc.* 126:12754–12755.
24. Jaroniec, C. P., B. A. Tounge, ..., R. G. Griffin. 2001. Frequency selective heteronuclear dipolar recoupling in rotating solids: accurate <sup>13</sup>C-<sup>15</sup>N distance measurements in uniformly <sup>13</sup>C, <sup>15</sup>N-labeled peptides. *J. Am. Chem. Soc.* 123:3507–3519.
25. Jaroniec, C. P., B. A. Tounge, ..., R. G. Griffin. 1999. Measurement of <sup>13</sup>C-<sup>15</sup>N distances in uniformly <sup>13</sup>C labeled biomolecules: J-decoupled REDOR. *J. Am. Chem. Soc.* 121:10237–10238.
26. deAzevedo, E. R., T. J. Bonagamba, ..., K. Schmidt-Rohr. 1999. Centerband-only detection of exchange: efficient analysis of dynamics in solids by NMR. *J. Am. Chem. Soc.* 121:8411–8412.
27. deAzevedo, E. R., S. B. Kennedy, and M. Hong. 2000. Determining slow motions in extensively labeled proteins by <sup>13</sup>C-detected <sup>15</sup>N exchange NMR. *Chem. Phys. Lett.* 321:43–48.
28. Bak, M., J. T. Rasmussen, and N. C. Nielsen. 2000. SIMPSON: a general simulation program for solid-state NMR spectroscopy. *J. Magn. Reson.* 147:296–330.
29. Veshkort, M., and R. G. Griffin. 2006. SPINEVOLUTION: a powerful tool for the simulation of solid and liquid state NMR experiments. *J. Magn. Reson.* 178:248–282.
30. Luo, W., and M. Hong. 2006. Determination of the oligomeric number and intermolecular distances of membrane protein assemblies by anisotropic <sup>1</sup>H-driven spin diffusion NMR spectroscopy. *J. Am. Chem. Soc.* 128:7242–7251.
31. Cady, S. D., T. V. Mishanina, and M. Hong. 2009. Structure of amantadine-bound M2 transmembrane peptide of influenza A in lipid bilayers from magic-angle-spinning solid-state NMR: the role of Ser<sup>31</sup> in amantadine binding. *J. Mol. Biol.* 385:1127–1141.
32. Hu, F., W. Luo, ..., M. Hong. 2011. Conformational plasticity of the influenza A M2 transmembrane helix in lipid bilayers under varying pH, drug binding, and membrane thickness. *Biochim. Biophys. Acta.* 1808:415–423.
33. Wang, J., S. Kim, ..., T. A. Cross. 2001. Structure of the transmembrane region of the M2 protein H<sup>+</sup> channel. *Protein Sci.* 10:2241–2250.
34. Pettersen, E. F., T. D. Goddard, ..., T. E. Ferrin. 2004. UCSF CHIMERA—a visualization system for exploratory research and analysis. *J. Comput. Chem.* 25:1605–1612.
35. Krieger, E., G. Koraimann, and G. Vriend. 2002. Increasing the precision of comparative models with YASARA NOVA—a self-parameterizing force field. *Proteins.* 47:393–402.
36. Bremi, T., and R. Bruschweiler. 1997. Locally anisotropic internal polypeptide backbone dynamics by NMR relaxation. *J. Am. Chem. Soc.* 28:6672–6673.
37. Andreas, L. B., M. T. Eddy, ..., R. G. Griffin. 2012. Magic-angle-spinning NMR of the drug resistant S<sup>31</sup>N M2 proton transporter from influenza A. *J. Am. Chem. Soc.* 134:7215–7218.
38. Can, T. V., M. Sharma, ..., T. A. Cross. 2012. Magic angle spinning and oriented sample solid-state NMR structural restraints combine for influenza A M2 protein functional insights. *J. Am. Chem. Soc.* 134:9022–9025.
39. Wang, T., S. D. Cady, and M. Hong. 2012. NMR determination of protein partitioning into membrane domains with different curvatures and application to the influenza M2 peptide. *Biophys. J.* 102:787–794.
40. Ma, C., A. L. Polishchuk, ..., L. H. Pinto. 2009. Identification of the functional core of the influenza A virus A/M2 proton-selective ion channel. *Proc. Natl. Acad. Sci. USA.* 106:12283–12288.
41. Mani, R., M. Tang, ..., M. Hong. 2006. Membrane-bound dimer structure of a  $\beta$ -hairpin antimicrobial peptide from rotational-echo double-resonance solid-state NMR. *Biochemistry.* 45:8341–8349.
42. Cady, S. D., K. Schmidt-Rohr, ..., M. Hong. 2010. Structure of the amantadine binding site of influenza M2 proton channels in lipid bilayers. *Nature.* 463:689–692.
43. Lovell, S. C., J. M. Word, ..., D. C. Richardson. 2000. The penultimate rotamer library. *Proteins.* 40:389–408.
44. Ma, J. C., and D. A. Dougherty. 1997. The cation- $\pi$  interaction. *Chem. Rev.* 97:1303–1324.
45. Lin, T. I., and C. Schroeder. 2001. Definitive assignment of proton selectivity and attoampere unitary current to the M2 ion channel protein of influenza A virus. *J. Virol.* 75:3647–3656.
46. Mould, J. A., J. E. Drury, ..., L. H. Pinto. 2000. Permeation and activation of the M2 ion channel of influenza A virus. *J. Biol. Chem.* 275:31038–31050.
47. Mould, J. A., H. C. Li, ..., L. H. Pinto. 2000. Mechanism for proton conduction of the M2 ion channel of influenza A virus. *J. Biol. Chem.* 275:8592–8599.
48. Yi, M., T. A. Cross, and H. X. Zhou. 2009. Conformational heterogeneity of the M2 proton channel and a structural model for channel activation. *Proc. Natl. Acad. Sci. USA.* 106:13311–13316.

## Supporting Information

### pH-Dependent Conformation, Dynamics, and Aromatic Interaction of the Gating Tryptophan Residue of the Influenza M2 Proton Channel from Solid-State NMR

Jonathan K. Williams, Yuan Zhang, Klaus Schmidt-Rohr and Mei Hong\*  
Department of Chemistry, Iowa State University, Ames, IA 50011

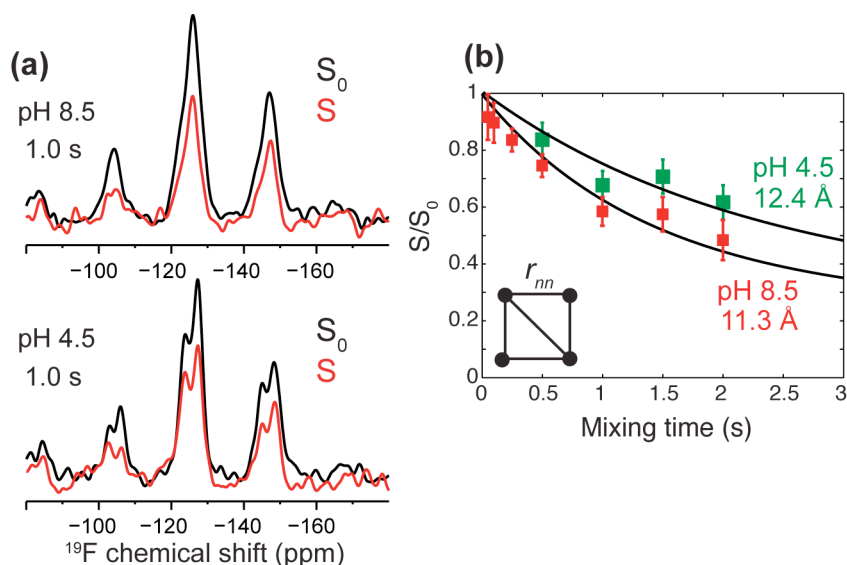


**Figure S1.**  $^{19}\text{F}$  CODEX spin diffusion data of 5- $^{19}\text{F}$ -labeled Trp41 in VM-bound M2TM. (a) Representative CODEX control ( $S_0$ ) and dephased ( $S$ ) spectra of the pH 8.5 and pH 4.5 samples under 8 kHz MAS. The spectra were measured at 200 K and 235 K without significant intensity differences. The mixing times were (b) Normalized  $S/S_0$  intensity as a function of mixing time. The high-pH sample shows faster decay than the low-pH sample, indicating shorter  $^{19}\text{F}$ - $^{19}\text{F}$  intermolecular distances. Best fits assuming a symmetric tetramer gave a nearest-neighbor distance of 11.3 Å for the high-pH sample and 12.4 Å for the low-pH sample.

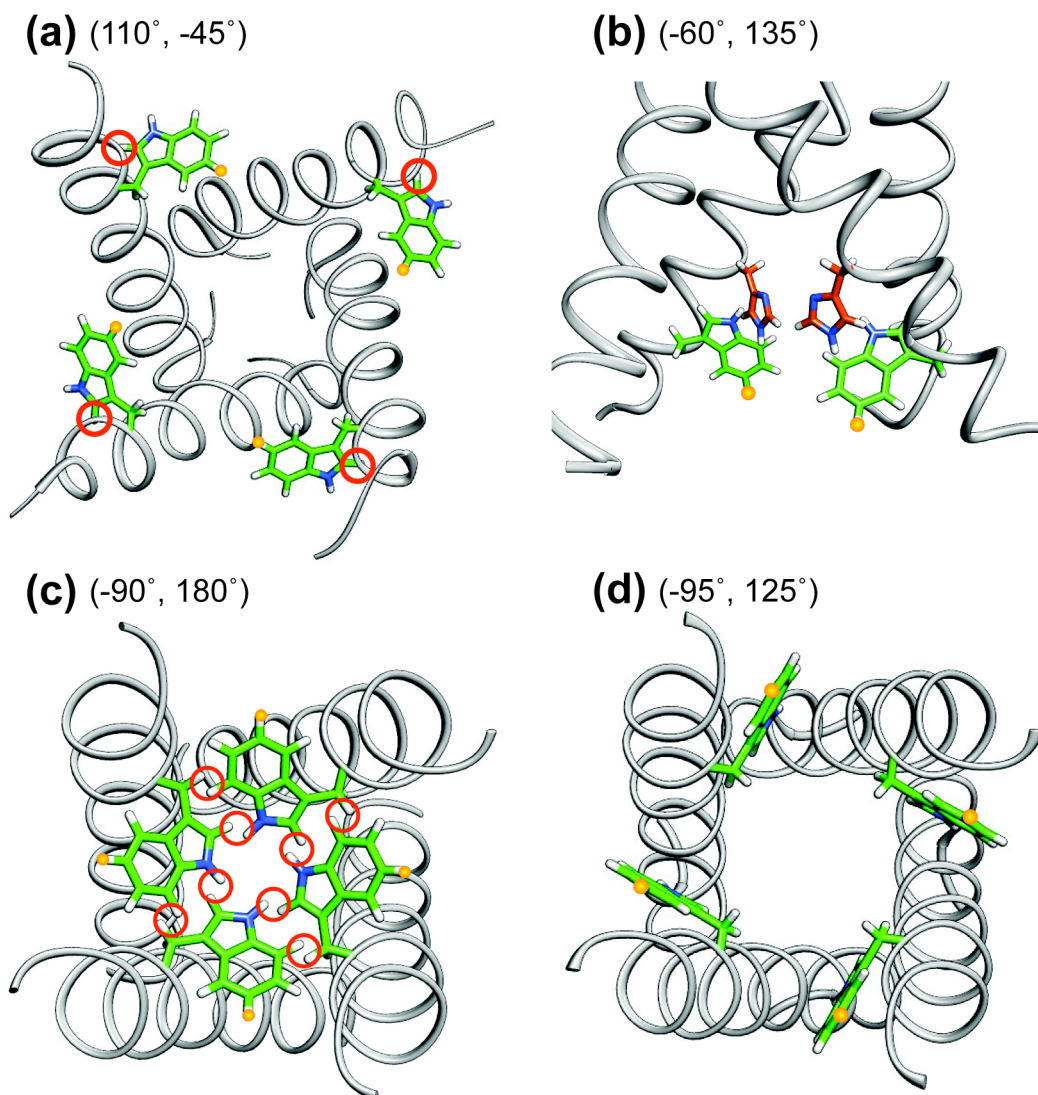


**Figure S2.** Examples of Trp41 ( $\chi_1$ ,  $\chi_2$ ) rotamers that are ruled out because of steric clash or low statistical probability. The 5-<sup>19</sup>F position (H $\zeta$ 3) is highlighted in orange. (a) 3C9J backbone with a Trp rotamer of (110°, -45°) has steric clash between the Trp41 C $\delta$ 1 and the helix backbone (red circles). (b) 3C9J backbone with a Trp rotamer of (-60°, 135°) has intrahelical steric clashes between the His37 N $\epsilon$ 2-H, C $\delta$ 2-H bonds and the Trp 41 C $\zeta$ 2-H, N $\epsilon$ 1-H bonds. For clarity only two of the four rings are shown for each residue. (c) 3LBW backbone with a Trp41 rotamer of (-90°, 180°) shows Trp-Trp clashes between N $\epsilon$ 1 and C $\delta$ 1, and between C $\beta$  and C $\zeta$ 2 of adjacent indole rings (red circles). (d) 2KQT backbone with a Trp rotamer (95°, -125°). This is rarely populated in  $\alpha$ -helices (~2%) (43).

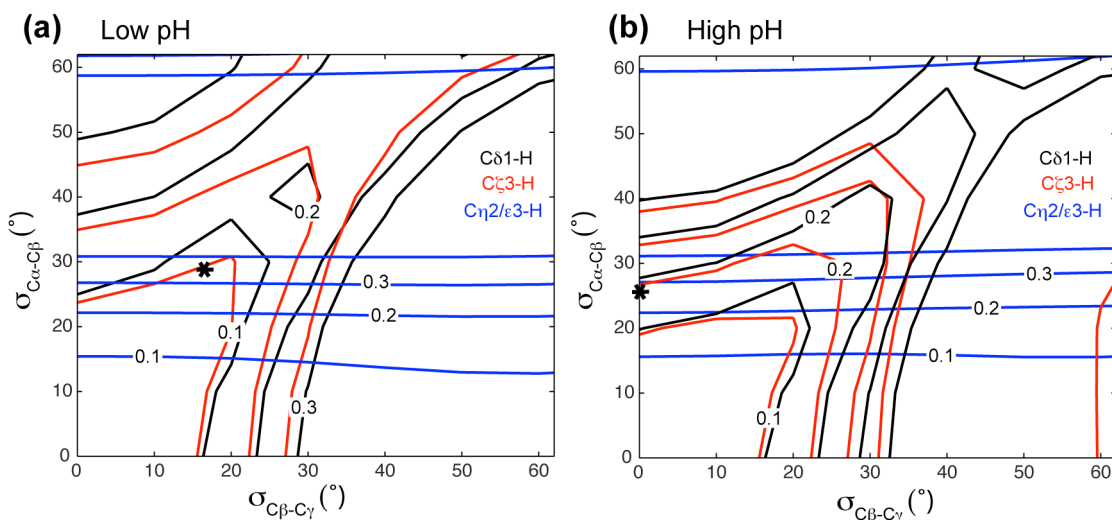


**Figure S3.** Motionally averaged asymmetry parameters  $\bar{\eta}$  as a function of the standard deviations of the Gaussian fluctuations around the  $C\alpha-C\beta$  and  $C\beta-C\gamma$  axes. Only asymmetry parameters between 0.1 and 0.4 are indicated for simplicity. (a) Low pH data, calculated using  $\chi_2=+135^\circ$ . (b) High pH data, calculated using  $\chi_2=+120^\circ$ . The position of the best-fit motional amplitudes at each pH is indicated with a cross. With these motional amplitudes, the averaged asymmetry parameters do not deviate significantly from 1. The  $C\delta 1-H$  and  $C\zeta 3-H$  couplings have an  $\bar{\eta}$  of less than 0.1 at low pH and about 0.2 at high pH. The  $C\eta 2/C\epsilon 3-H$  couplings have a modestly larger  $\bar{\eta}$  of 0.3. Within experimental uncertainty, these small  $\bar{\eta}$  values are not detected in the C-H dipolar dephasing curves, and the uniaxial approximation is reasonable for estimating the order parameters from the experimental data.

## New and Notable

### The Functional Heart of the M2 Channel

Sebastian Hiller\*

Biozentrum, University of Basel, Basel, Switzerland

The equilibration of pH between external environment and viral interior is an essential part of the influenza virus lifecycle. After infection of a eukaryotic cell, the virus needs to transmit protons across its lipidic envelope from the acidic exterior, an endosome, to the interior, eventually triggering unpacking of the viral genome (1). This essential function is fulfilled by the viral protein M2 channel, a tetrameric assembly of four transmembrane helices. The proton pore is formed in the center of the four helices. Two amino-acid residues in the pore are crucial for function, forming a HxxxW motif: Histidine 37 provides for the selectivity and Tryptophan 41 for the pH-dependent gating. Structure, conformation, and mechanism of the M2 channel and in particular of these two residues are subject to intense ongoing research (2).

In this issue of *Biophysical Journal*, Williams et al. (3) use solid-state NMR spectroscopy to determine the orientation of the Trp<sup>41</sup> side chain in the low and the high pH states of the M2 channel. So far, 10 different structures have been deposited in the Protein Data Bank database, determined by different techniques: solid-state NMR spectroscopy, solution NMR spectroscopy, and x-ray crystallography (4–13). These 10 structures feature, however, a total of three different rotamers for the Trp<sup>41</sup> chain. Williams et al. (3) now employ solid-state NMR distance measurements between selected nuclei in specifically isotope-

labeled samples to distinguish between the rotameric Trp<sup>41</sup> orientations. Importantly, the channel is reconstituted in native-like lipid bilayers for the solid-state magic-angle spinning NMR experiments.

The proton conductance mechanism of the M2 channel had previously been determined. In the high pH closed state, the four His<sup>37</sup> side chains block the channel by forming a  $\pi$ -stacked structure. At low pH, however, the His<sup>37</sup> cluster is conductive, due to fast protonation and deprotonation as part of a proton wire (14,15). Together with these previous experiments, the orientation of the Trp side chain can now further explain the conducting and gating mechanism of the M2. Trp<sup>41</sup> is found to adopt a *t*90 rotamer in both pH states, with 20° difference in  $\chi_1$  and  $\chi_2$  between the high and low pH states. Additional measurements determine the amplitudes of the Trp side-chain dynamics, showing increased fluctuations at low pH. Importantly, His<sup>37</sup> and Trp<sup>41</sup> approach each other closely at low pH by a cation- $\pi$  interaction. This close interaction provides the structural basis for the gating by Trp, as it reduces the proton dissociation rate from His<sup>37</sup> to water from  $4.5 \times 10^5 \text{ s}^{-1}$  to <1% thereof. Furthermore, the Trp gate, which is located toward the virus interior, blocks the accessibility of protons to the His gate and thus results in the overall unidirectional proton conductance. Overall, the visualization of the measured amplitudes of the two side chains pumping protons through the M2 channel by their reorientation evokes the visual analogy of a stroking heart that pumps blood through its valves (Fig. 7 of Williams et al. (3)).

Determination of amino-acid side-chain rotamers is a fundamental biophysical challenge, often necessary to understand protein function at atomic detail. Specific solid-state NMR experiments, such as the REDOR (16) and CODEX (17) experiments used here, in combination with suitable isotope labeling schemes are central

techniques in the ongoing work of Luo and Hong (18), Luo et al. (19), Hong et al. (20), and Wang et al. (21). This article demonstrates the potential of solid-state NMR to determine conformation and dynamics of amino-acid side chains at atomic resolution in the functional center of a membrane protein, outlining a procedure to be carried out also on larger and more complex membrane protein systems.

### REFERENCES

1. Helenius, A. 1992. Unpacking the incoming influenza virus. *Cell*. 69:577–578.
2. Cross, T. A., H. Dong, ..., H. X. Zhou. 2012. M2 protein from influenza A: from multiple structures to biophysical and functional insights. *Curr. Opin. Virol.* 2:128–133.
3. Williams, J. K., Y. Zhang, ..., M. Hong. 2013. pH-Dependent conformation, dynamics, and aromatic interaction of the gating tryptophan residue of the influenza M2 proton channel from solid-state NMR. *Biophys. J.* 104: 1698–1708.
4. Sharma, M., M. Yi, ..., T. A. Cross. 2010. Insight into the mechanism of the influenza A proton channel from a structure in a lipid bilayer. *Science*. 330:509–512.
5. Hu, J., T. Asbury, ..., T. A. Cross. 2007. Backbone structure of the amantadine-blocked trans-membrane domain M2 proton channel from Influenza A virus. *Biophys. J.* 92:4335–4343.
6. Nishimura, K., S. Kim, ..., T. A. Cross. 2002. The closed state of a H<sup>+</sup> channel helical bundle combining precise orientational and distance restraints from solid state NMR. *Biochemistry*. 41:13170–13177.
7. Pielak, R. M., J. R. Schnell, and J. J. Chou. 2009. Mechanism of drug inhibition and drug resistance of influenza A M2 channel. *Proc. Natl. Acad. Sci. USA*. 106:7379–7384.
8. Pielak, R. M., and J. J. Chou. 2010. Solution NMR structure of the V27A drug resistant mutant of influenza A M2 channel. *Biochem. Biophys. Res. Commun.* 401:58–63.
9. Schnell, J. R., and J. J. Chou. 2008. Structure and mechanism of the M2 proton channel of influenza A virus. *Nature*. 451:591–595.
10. Acharya, R., V. Carnevale, ..., M. L. Klein. 2010. Structure and mechanism of proton transport through the transmembrane tetrameric M2 protein bundle of the influenza A virus. *Proc. Natl. Acad. Sci. USA*. 107: 15075–15080.
11. Stouffer, A. L., R. Acharya, ..., W. F. DeGrado. 2008. Structural basis for the

Submitted February 13, 2013, and accepted for publication March 7, 2013.

\*Correspondence: [sebastian.hiller@unibas.ch](mailto:sebastian.hiller@unibas.ch)

Editor: Paulo Almeida.

© 2013 by the Biophysical Society  
0006-3495/13/04/1639/2 \$2.00



- function and inhibition of an influenza virus proton channel. *Nature*. 451:596–599.
12. Cady, S. D., K. Schmidt-Rohr, ..., M. Hong. 2010. Structure of the amantadine binding site of influenza M2 proton channels in lipid bilayers. *Nature*. 463:689–692.
  13. Cady, S. D., T. V. Mishanina, and M. Hong. 2009. Structure of amantadine-bound M2 transmembrane peptide of influenza A in lipid bilayers from magic-angle-spinning solid-state NMR: the role of Ser<sup>31</sup> in amantadine binding. *J. Mol. Biol.* 385:1127–1141.
  14. Hu, F., W. Luo, and M. Hong. 2010. Mechanisms of proton conduction and gating in influenza M2 proton channels from solid-state NMR. *Science*. 330:505–508.
  15. Hu, F., K. Schmidt-Rohr, and M. Hong. 2012. NMR detection of pH-dependent histidine-water proton exchange reveals the conduction mechanism of a transmembrane proton channel. *J. Am. Chem. Soc.* 134: 3703–3713.
  16. Gullion, T., and J. Schaefer. 2011. Rotational-echo double-resonance NMR. *J. Magn. Reson.* 81:413–417.
  17. Hu, W. G., T. J. Bonagamba, and K. Schmidt-Rohr. 1999. Centerband-only detection of exchange: efficient analysis of dynamics in solids by NMR. *J. Am. Chem. Soc.* 121:8411–8412.
  18. Luo, W., and M. Hong. 2006. Determination of the oligomeric number and intermolecular distances of membrane protein assemblies by anisotropic <sup>1</sup>H-driven spin diffusion NMR spectroscopy. *J. Am. Chem. Soc.* 128: 7242–7251.
  19. Luo, W., R. Mani, and M. Hong. 2007. Side-chain conformation of the M2 transmembrane peptide proton channel of influenza A virus from <sup>19</sup>F solid-state NMR. *J. Phys. Chem. B.* 111:10825–10832.
  20. Hong, M., T. V. Mishanina, and S. D. Cady. 2009. Accurate measurement of methyl <sup>13</sup>C chemical shifts by solid-state NMR for the determination of protein side chain conformation: the influenza A M2 transmembrane peptide as an example. *J. Am. Chem. Soc.* 131:7806–7816.
  21. Wang, T., S. D. Cady, and M. Hong. 2012. NMR determination of protein partitioning into membrane domains with different curvatures and application to the influenza M2 peptide. *Biophys. J.* 102:787–794.